Title
Neural–metabolic coupling in the central visual pathway

Journal
Philosophical Transactions of the Royal Society B Biological Sciences, 371(1705)

ISSN
0962-8436

Authors
Freeman, Ralph D
Li, Baowang

Publication Date
2016-10-05

DOI
10.1098/rstb.2015.0357

Peer reviewed

PHILOSOPHICAL TRANSACTIONS B

rstb.royalsocietypublishing.org

Review

Cite this article: Freeman RD, Li B. 2016 Neural–metabolic coupling in the central visual pathway. *Phil. Trans. R. Soc. B* **371**: 20150357.
http://dx.doi.org/10.1098/rstb.2015.0357

Accepted: 18 April 2016

One contribution of 15 to a Theo Murphy meeting issue 'Interpreting BOLD: a dialogue between cognitive and cellular neuroscience'.

Subject Areas:
neuroscience, cellular biology

Keywords:
visual system, tissue oxygen, neural activity, glucose, lactate, blood flow

Author for correspondence:
Ralph D. Freeman
e-mail: rfreeman@berkeley.edu

Neural–metabolic coupling in the central visual pathway

Ralph D. Freeman and Baowang Li

Group in Vision Science, School of Optometry, Helen Wills Neuroscience Institute, University of California, Berkeley, CA 94720-2020, USA

Studies are described which are intended to improve our understanding of the primary measurements made in non-invasive neural imaging. The blood oxygenation level-dependent signal used in functional magnetic resonance imaging (fMRI) reflects changes in deoxygenated haemoglobin. Tissue oxygen concentration, along with blood flow, changes during neural activation. Therefore, measurements of tissue oxygen together with the use of a neural sensor can provide direct estimates of neural–metabolic interactions. We have used this relationship in a series of studies in which a neural microelectrode is combined with an oxygen micro-sensor to make simultaneous co-localized measurements in the central visual pathway. Oxygen responses are typically biphasic with small initial dips followed by large secondary peaks during neural activation. By the use of established visual response characteristics, we have determined that the oxygen initial dip provides a better estimate of local neural function than the positive peak. This contrasts sharply with fMRI for which the initial dip is unreliable. To extend these studies, we have examined the relationship between the primary metabolic agents, glucose and lactate, and associated neural activity. For this work, we also use a Doppler technique to measure cerebral blood flow (CBF) together with neural activity. Results show consistent synchronously timed changes such that increases in neural activity are accompanied by decreases in glucose and simultaneous increases in lactate. Measurements of CBF show clear delays with respect to neural response. This is consistent with a slight delay in blood flow with respect to oxygen delivery during neural activation.

This article is part of the themed issue 'Interpreting BOLD: a dialogue between cognitive and cellular neuroscience'.

1. Background

A primary challenge in the use of non-invasive brain imaging is to enable broader and more fundamental applications than a limited topographical analysis. The identification of brain functions in both normal and abnormal neuronal systems would represent a significant increase in utility of neural imaging. For this to occur, it is necessary to have a detailed understanding of neural implications of the measurements that are made. Currently, functional magnetic resonance imaging (fMRI) is the most developed approach. In this method, blood oxygenation level-dependent (BOLD) signals are used to infer neural activity. However, there remain basic questions regarding the relationships between BOLD signals and neural function. The BOLD signal is sensitive to oxygen extraction fraction (OEF), the percentage of oxygen removed from the blood by tissue during its passage through the capillary network. The BOLD signal is not necessarily linked to neural activity if there are matched fractional changes in cerebral metabolic rate of oxygen ($CMRO_2$) and cerebral blood flow (CBF), which results in no change in the OEF. However, fMRI is a powerful technique because in an activated brain area, blood flow increases much more than oxygen metabolic rate [1,2]. This leads to a reduction in the OEF, which contributes to a local increase in the magnetic resonance signal during activated neural activity. These processes have been reviewed previously [3,4]. For the studies we report here, it is important to note that the BOLD signal depends mainly on changes in the concentration of deoxygenated

THE ROYAL SOCIETY PUBLISHING

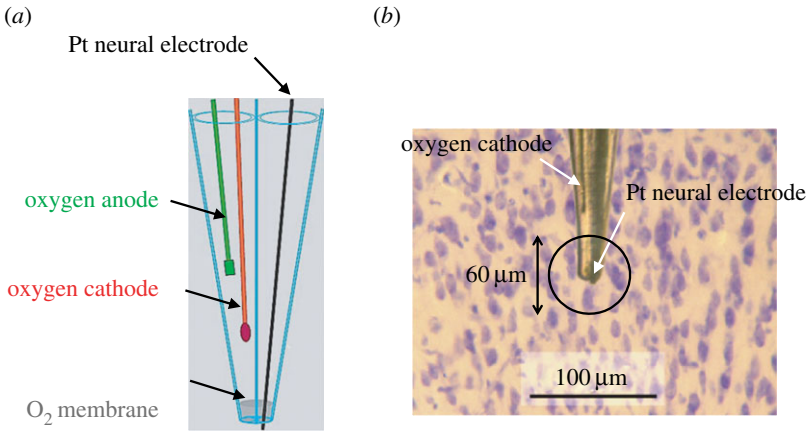

Figure 1. A dual neural–metabolic sensor. (*a*) A schematic configuration of the sensor. A neural microelectrode and an oxygen micro-sensor are enclosed in a double-barrel glass pipette. The tip of the neural electrode extends through the oxygen permeable membrane into tissue. The neural electrode and oxygen cathode are made of platinum. The oxygen anode is a silver–silver chloride reference electrode. (*b*) The sensor is displayed in brain tissue showing Golgi stained cells in the primate visual cortex. The spherical sensing field of the sensor is approximately 60 µm in diameter.

haemoglobin. This means that tissue oxygen consumption provides a direct estimate of the metabolic state of the particular brain region under study. Therefore, tissue oxygen concentration changes along with those of blood flow provide fundamental information about the neural state.

Details have emerged concerning the relationships of vascular and oxygen parameters during different stages of development of non-invasive neural imaging. In positron emission tomography (PET), CBF and $CMRO_2$ were reported to be coupled during inactivity but substantially dissociated during brain stimulation [1,2]. The assumption for the mismatch was anaerobic glycolysis, but subsequent studies found substantial $CMRO_2$ responses and increases in deoxygenated haemoglobin [5–9]. It should be mentioned that neural activity is accompanied by relatively large changes in CBF compared with those of $CMRO_2$. This decreases the concentration of deoxyhaemoglobin, which yields a BOLD response. With neural activity, CBF increase reduces deoxyhaemoglobin while $CMRO_2$ has the opposite effect. Relative changes in CBF and $CMRO_2$ affect BOLD response levels, and coupling properties are directly relevant. It is also necessary to note that neural activity includes membrane and spiking processes, facilitation and suppression, and various synaptic functions which are presumed to affect both CBF and $CMRO_2$ [10–13]. Although details of these processes remain to be established, for the purpose of the investigations to be described here, it is sufficient to point out that tissue oxygen is closely related to the BOLD signal. With neural activation, oxygen metabolism is increased along with that of CBF. This increases tissue oxygen concentration and causes a decrease in deoxyhaemoglobin. The BOLD signal is then increased because it is inversely related to the level of deoxyhaemoglobin. This increase is the primary measurement in fMRI.

Although CBF and $CMRO_2$ are of basic interest in the process of non-invasive neural imaging, their measurements in behaving organisms are not straightforward. However, it is possible to measure local concentrations of tissue oxygenation in activated brain tissue of a behaving animal. This may be done with a polarographic microelectrode to measure oxygen partial pressure in bulk solution or tissue oxygen concentration [14–16]. The device consists of a platinum cathode and a non-polarized anode. Sensor current is proportional to the concentration of tissue oxygen, and response time varies with size of the exposed platinum surface. A small surface yields rapid electrode responses to altered oxygen tensions. Area of sensitivity is approximately twice the diameter of the electrode tip.

In the studies described here [17–25], we have updated and modified the original design to incorporate a system that enables simultaneous co-localized measurements of tissue oxygen concentration changes during extracellular neural responses of activated cells in the central visual pathway. A schematic of the sensing device we have used is given in figure 1. A double-barrel glass pipette contains a neural microelectrode and an oxygen sensor, both made of platinum, as illustrated. The tip of the electrode extends through an oxygen permeable membrane into neural tissue. The oxygen sensor consists of an anode and cathode. The anode is a silver–silver chloride reference electrode. Tip size is around 30 µm and the field of sensitivity is around 60 µm. Oxygen sensor response time is less than 1 s. Impedance of the platinum neural electrode is from 0.5 to 2 MΩ.

We have used an anaesthetized cat preparation for which there is a history of extensive neurophysiological study that has provided detailed information concerning neural organization of the central visual pathway. In general, the neural system of the cat behaves like that of a scaled down primate. The intention of this work is to monitor neural–metabolic coupling in an intact system during visual processing in order to gain insights that are relevant to non-invasive neural imaging.

2. Neural–metabolic response characteristics of cortical cells

As visual processing progresses from early to central stages, two primary response characteristics emerge, orientation selectivity and ocular dominance. Cells in primary visual cortex are generally sensitive to specific limited ranges of orientation of visual stimuli. And these cells are also the first stage of processing where left and right eye information is functionally combined [26,27]. Data in figure 2 are presented to illustrate and compare neural and metabolic responses, which demonstrate orientation selectivity [22].

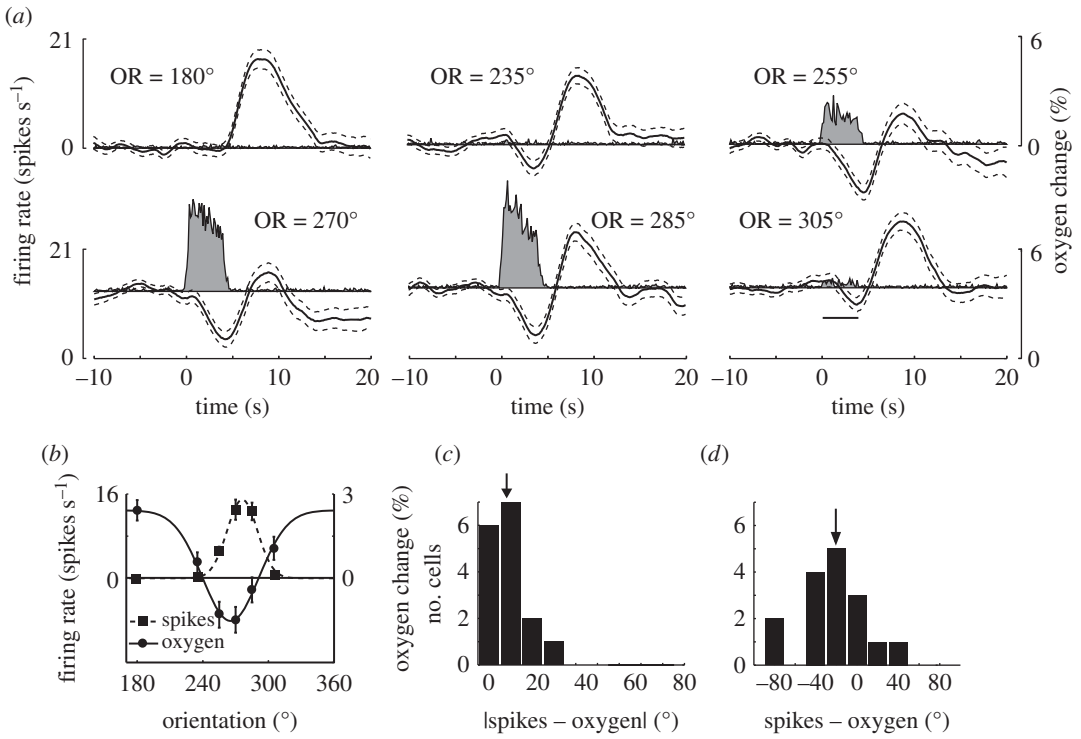

Figure 2. Orientation selectivity of neural and tissue oxygen responses in visual cortex. (*a*) Neural and tissue oxygen responses to visual stimuli of different orientations for a representative recording site. Data are averaged responses across 72 trials. Oxygen responses are quantified as percentage change from baseline signals. Dashed lines represent $\pm$ 1 s.e.m. (*b*) Orientation tuning curves of neural and tissue oxygen responses. The oxygen level is determined when oxygen and neural responses show maximum correlation (5.75 s after stimulus onset) for each orientation condition. Neural responses are quantified as the average spiking rates during the stimulus. Spontaneous activity is subtracted from neural responses for each orientation condition. Oxygen response is quantified as the percentage change from the baseline occurring 5.75 s after stimulus onset. Note that this time gives the best correlation between spike rate and tissue oxygenation for the group of data. Average spike and oxygen responses are fit to independent Gaussian functions. Error bars represent $\pm$ 1 s.e.m. (*c*,*d*) Comparison of orientation selectivity between neural and oxygen responses for a group of recording sites ($n = 16$). Distributions of differences in preferred orientation (*c*) and tuning width (*d*) are shown between neural and oxygen responses. Downward arrows indicate mean values.

First, the neural response range for this cell is limited to around a 30° range between 255° and 285° (figure 2*a*). Within that range, neural response is vigorous. Correspondingly, tissue oxygen level changes occur for all orientations but the curves have different forms. Within the range of neural firing, there are clear biphasic oxygen responses with substantial initial negative dips followed by generally moderate secondary peaks. The biphasic oxygen response is typical for most of our measurements. It is possible that the initial negative dip represents an immediate oxygen utilization and the positive secondary peak could be the result of blood flow that follows the oxygen response. These notions are speculative and there are discussions in the literature in which it is proposed that blood flow is immediate [28,29]. The other feature that is notable in figure 2*a* is that orientations removed from those that yield neural responses have substantial secondary peaks in oxygen changes. This is somewhat counterintuitive and we believe that the secondary peaks represent activity in multiple orientation columns beyond those that are detectable by the neural electrode. The implication is that the initial dip is a better indicator of local neural response activity and we have found evidence consistent with this view [22–24,30]. In summary, there is a close correspondence between initial dip oxygen change and neural activity within a preferred orientation range. However, the potential use of the initial dip for fMRI is limited because it is not reliable [31,32].

As shown in figure 2*a*, a strong neural response is indicated in conjunction with the negative oxygen dip. The test results for orientations away from optimal show decreases in both neural response and initial dip up to the orthogonal orientation for which there is no neural response and a relatively large secondary positive oxygen change. Tuning curves for the same cell, shown in figure 2*b*, exhibit well-matched inverse tuning characteristics. Summaries for a small group of cells ($n = 16$), given in figure 2*c*,*d*, include, respectively, differences between neural and oxygen parameters for optimal orientations and for tuning widths. Respective mean differences between neural and oxygen values (arrows, figure 2*c*,*d*) for these parameters are relatively modest.

Analogous data for ocular dominance are presented in figure 3*a* for the same example cell as shown in figure 2. Ocular dominance refers to the condition in which a given cortical cell is differentially driven by left and right eyes. For some cells, the two eyes are equally effective. For others, one eye dominates a cell by varying degrees. And some cells are driven only monoptically. For the current cell, left eye activation is stronger for both the neural and tissue oxygen responses (figure 3*a*). Graphical representation (figure 3*b*) shows response values for spike count and oxygen change. The left eye exhibits a negative oxygen change in correspondence with a relatively strong neural response. A summary, shown in figure 3*c* for 21 cells, plots right and left eye differences in oxygen tension versus relative neural ocular dominance. The clearly inverse relationship between the two variables is consistent with relatively large negative oxygen changes for the eye, which elicits stronger neural responses. This result is consistent with previous studies [30,33,34] which suggest that oxygen changes may be localized within a cortical column.

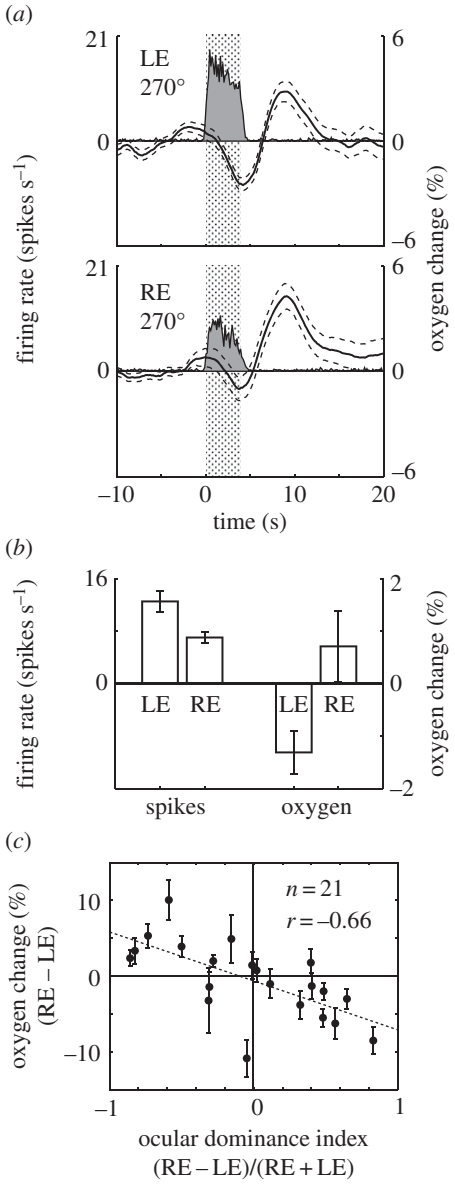

Figure 3. Ocular dominance values of neural and oxygen responses. (*a*) Neural and oxygen responses for the same recording site as in figure 2 are shown for left eye ((*a*), top) and right eye ((*a*), bottom) stimulation. (*b*) Bar plots compare the average neural and oxygen responses (5.75 s after stimulus onset) between the two eyes. (*c*) The difference in oxygen change between the two eyes is plotted as a function of the ocular dominance index for a population of recording sites ($n = 21$). Each filled circle represents a recording site.

3. Characteristics of tissue oxygen and neural responses to visual stimuli

Responses to visual stimuli have been studied in detail at most stages of the central visual pathway. However, the data obtained are mainly limited to neuronal processes. Parallel metabolic characteristics are generally not available. Experiments described in this section are intended to provide some of this information. As described in §2, typical tissue oxygen responses are biphasic. A small initial negative dip is followed by a relatively large positive peak. As noted in §2, the first phase may reflect immediate usage of oxygen and the second could represent increased blood flow, which is slightly delayed because of draining veins and the initiation of hyperaemia. The relative roles of CBF and $CMRO_2$, in timing or in magnitude, are not clear [35]. To address this area, we have made neural–metabolic recordings in the lateral geniculate nucleus (LGN) [17,19,23,24] in addition to visual cortex. The dorsal LGN receives direct input from retinal ganglion cells and projects to primary visual cortex. What makes it useful for the present purpose is that it exhibits precise retinotopic organization and has small receptive field size. LGN cells also produce strong responses to visual stimuli, which can be accurately measured with spatial precision.

A simple test of spatial parameters for LGN cells may be explored as follows. A sinusoidal grating can be used as a stimulus to find correct receptive field variables. The size and parameters of the stimulus can be adjusted to match receptive field dimensions and requirements. In general, LGN cells have small receptive fields and high firing rates for optimal gratings. For many LGN cells that we have tested, the smallest stimulus elicits vigorous neural activity and strong monophasic negative oxygen responses. As stimulus size increases, neural response remains strong or is slightly reduced while the initial negative oxygen response becomes smaller and a secondary positive phase emerges. Tests with various sized grating stimuli either covering or positioned outside the receptive field indicate that the negative dip in oxygen responses is clearly coordinated with strong neural activity. This indicates that oxygen consumption is highly specific to local changes in neural activity. The monophasic negative oxygen responses may reflect increases in $CMRO_2$ and the positive changes could be associated with CBF. The oxygen changes are localized with neural activity but at relatively larger spatial scales.

An extension of these tests can be made to explore the spatial selectivity of the negative oxygen response. Once again, LGN cells are recorded using stimuli that are at first coincident with the receptive field dimensions, and then moved spatially so that they are located at positions that are offset from the centre. For these trials, as the grating stimuli are progressively displaced from the centre of the receptive field, the oxygen initial dip response becomes smaller. These results are consistent with the finding that activity induced oxygen consumption is well localized to the site of neuronal responses. Finally, calculated point spread functions of biphasic tissue oxygen responses in LGN show that negative response components are substantially narrower than those for positive phases [24]. These data are consistent with previous findings suggesting that early hemodynamic responses are related to increases in $CMRO_2$ [30]. The initial negative dip in oxygen tension appears to be spatially highly specific whereas the secondary positive peak, which may represent CBF activity, appears to be based on a relatively large region. If applied to fMRI, the initial dip would be a better estimate of local neural function. However, as noted in §2, it is well known that the initial dip in fMRI is elusive, variable, weak and may be completely missing in standard measurements [31,32]. This is relevant here because initial dip data in our experiments are generally very robust and reliable.

4. Temporal and spatial summation

The results presented above show that negative tissue oxygen response changes are coupled with neural activity in a closely localized manner. To obtain details concerning oxygen response characteristics, we have conducted tests in which stimulus size can be temporally or spatially altered to evaluate

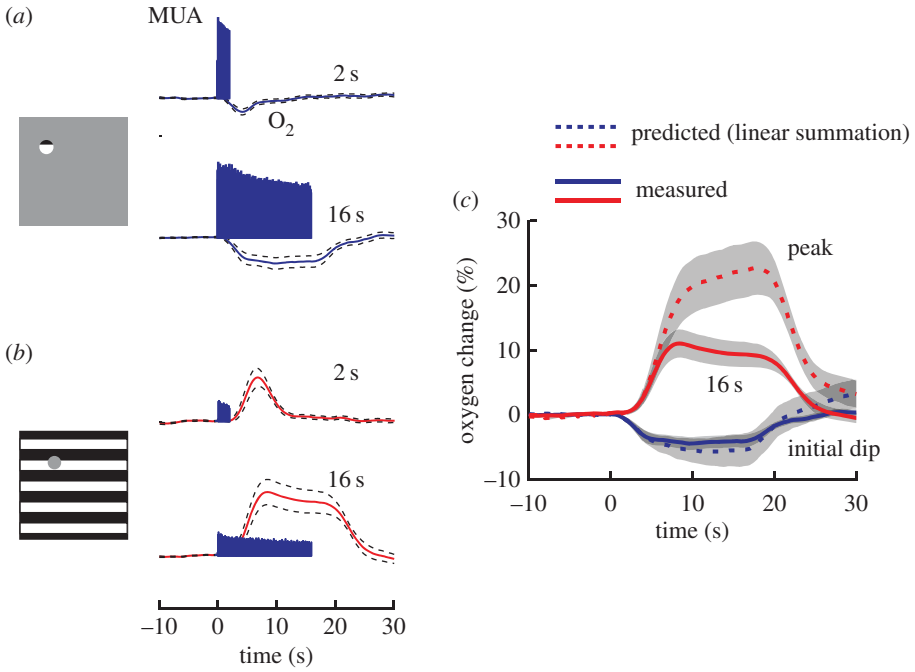

Figure 4. Degree of temporal linearity of neurometabolic coupling in the LGN. (*a*,*b*) Neural and oxygen responses to visual stimuli of different durations (2 and 16 s) for a representative recording site. A small stimulus is centred over the receptive field (*a*), and a full-field stimulus with a blank mask covering the receptive field of the recording site (*b*). Dashed lines represent ±1 s.e.m. (*c*) Estimation of temporal linearity of tissue oxygen response. Predicted responses to long-duration stimuli are generated by replicating, shifting, and summing measured responses to short-duration stimuli. Blue and red lines indicate responses to small and large stimuli, respectively. Large stimulus contains mask over receptive field. Measured and predicted oxygen responses to 16 s stimuli based on 2 s stimuli are shown in solid and dashed lines, respectively.

the relative linearity of these variables [17,19]. To do this, visual stimuli with different durations and spatial patterns were presented, while activity from LGN cells was monitored. A test of temporal integration is illustrated in figure 4. For a small grating stimulus at a size that matches the receptive field dimension (figure 4*a*), multiple unit activity (MUA) along with the oxygen tension change is shown for a 2 s duration presentation. A similar response set is given also for a 16 s stimulus. Another set of data are shown below (figure 4*b*) for the same LGN location. In this case, the grating is large and contains a blank mask centred over the receptive field. Here, neural responses are minimal, as expected, and there are prominent positive oxygen changes at both 2 and 16 s durations. To examine the degree of temporal linearity for both the negative and positive oxygen components, we included other stimuli of 4 and 8 s durations (not included in figure 4). We then used short presentation data to predict summated responses. For example, we summated a 2 s response with that of a 2 s right-shifted response to predict a 4 s result and compared it with the measured 4 s response. Data for one prediction, for a 16 s presentation, are shown in figure 4*c*. The initial dip data (blue lines) show a close correlation between measured and predicted results suggesting a linear metabolic temporal summation. On the other hand, there is a considerable discrepancy between measured and predicted results for the positive oxygen response (red lines). Predictions yield considerably larger values than measured results. This over-estimation of a positive oxygen response is consistent with nonlinear temporal summation of the BOLD signal in fMRI [36–38]. If the positive oxygen response is due mainly to an increase in CBF, nonlinear neurovascular coupling will affect the BOLD signal.

An analogous set of tests to those described above is used to explore the extent of spatial integration. To do this, we use the observation that the classical receptive field has an additional region surrounding it that can influence responses even though direct stimulation there cannot excite a neuron. We have conducted tests in both LGN and visual cortex using the following stimuli [19]. First, optimal stimulus parameters are determined for a given cell. They are then used for a grating patch consisting of a pattern within a full circle that matches classical receptive field size. Full size, a left and a right half semicircle size are used as depicted in figure 5*a–c*. Two additional larger stimuli (figure 5*d*,*e*) are used which consist of full-field gratings, one of which contains a blank mask covering the classical receptive field. Tests using these five stimulus patterns were made at an LGN recording site and the data obtained are shown in the middle and right columns for oxygen changes and neural activity profiles, respectively. In figure 5*c*,*e*, predicted composite data are included with measured results to examine linearity of spatial summation. This test sequence covers characteristics of spatial summation both within the classical receptive field and in the surrounding region. The oxygen data (middle column) show clear initial dips for each half circle grating and a larger negative change for the full circle stimulus. For the larger stimuli extending beyond the classical receptive field there are minimal initial dips and pronounced secondary positive peaks. The neural data (right column) show responses for each half grating stimulus and a larger response for the full grating in accord with the oxygen data. The large grating stimulus outside the classical receptive field yields only a small amount of spontaneous activity when a blank mask covers the centre, as expected. When the mask is removed, the extended grating yields a response that is reduced in comparison with that for the classical receptive field. Predicted composite responses for the full circle grating are greater than the measured values for both oxygen and

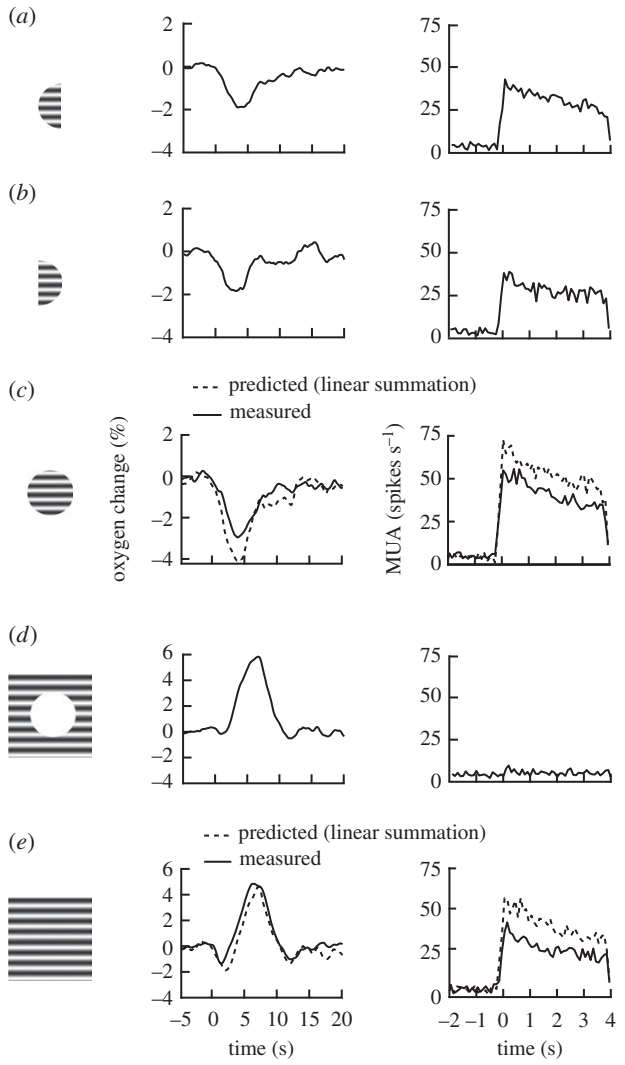

Figure 5. Degree of spatial linearity of neurometabolic coupling in the LGN. (*a–c*) Tissue oxygen and neural responses to visual stimuli of different spatial patterns within the receptive field for a recording site. A left semicircular stimulus (*a*), a right semicircular stimulus (*b*), and a full circular stimulus (*c*) are centred on the receptive field. Optimal receptive field size stimuli are used, and the sum of those in (*a*) and (*b*) is equal to that in (*c*). Oxygen and neural responses are shown in middle and right columns, respectively. (*d*) A full-field stimulus with a blank mask covering the receptive field is used to stimulate the surround. (*e*) A full-field stimulus. Summation of the stimuli in (*c*) and (*d*) matches the full-field stimulus (*e*). Data are averaged over 32 trials. Black and dashed curves in (*c*) and (*e*) represent measured and predicted composite oxygen and neural responses to the full circular receptive field stimulus (*c*) and the full-field stimulus (*e*), respectively.

neural data. For the full-field response, predicted and measured values are similar for positive oxygen peaks but predicted neural responses are higher than those measured.

Population data from LGN also show nonlinearity of spatial summation. Within the classical receptive field, composite predicted oxygen and neural responses are substantially larger than measured values. Impulse response function estimates indicate a neural basis for the nonlinear spatial summation of tissue oxygen levels within the classical receptive field. For the surrounding area, predicted oxygen responses have relatively large initial dips but similar positive peaks in comparison with measured values. Predicted composite spiking activity is also substantially stronger than measured levels. This suggests a nonlinear coupling between oxygen and neural responses when spatial summation is examined. Considered together, these findings suggest that oxygen initial dip values and neural activity are closely coupled in both space and time.

5. Binocular activation

Binocular activation of the visual pathway is relevant to the study of neural–metabolic coupling as it may provide insights regarding interpretation of haemodynamic signals. A primary question regarding interpretation of BOLD signals concerns the neural nature of the measurement that is represented. Specifically, synaptic activity is considered to be the input stage, and spiking discharge the output of neural response. These components are obviously related, but previous work suggests that synaptic activity may be more directly reflected in the BOLD response [39]. Both CBF and $CMRO_2$ are presumably involved, but measurements of these factors in an *in vivo* functioning neural system are difficult to make. The oxygen and neural co-localized measurements we describe here provide a way to activate and compare inhibitory and excitatory neural processes in the visual cortex. This allows us to compare metabolic, spiking and local field potential responses during excitatory or inhibitory binocular interaction.

To obtain these data, drifting sinusoidal gratings were presented to both eyes simultaneously on two cathode ray tube monitors. Preferred grating specifications were determined and dichoptic tests were run such that phase was fixed in one eye and variable for the other [20]. This provided response data for a series of randomly interleaved relative interocular phase values. This sequence is equivalent to relative binocular disparities. The dual neural–metabolic sensor described above was used here to monitor tissue oxygen responses in visual cortex while MUA, and local field potentials (LFP) were measured. The LFP frequency range we focused on was between 25 and 115 Hz (gamma range) as in previous work [25,39,40]. Representative results are presented in figure 6 for MUA, LFP (gamma frequencies), and oxygen response data for six relative interocular phases interleaved with a control stimulus presented monoptically to the dominant eye. In the first profile (figure 6*a*), MUA responses vary with interocular phase and peak at around 240°. The MUA data show a typical phase-specific binocular interactive profile in which spiking activity varies from below to above the monocular control level. There is clear statistically significant facilitation and suppression exhibited in this response as shown in previous work [27,41,42]. By contrast, LFP power (figure 6*b*) varies and is relatively strong at all phase values. And initial dip oxygen responses (figure 6*c*) are also slightly variable and, as in the LFP case, are all larger than those of the monocular control. The positive peak oxygen data (figure 6*d*) exhibit phase tuning that is different than that for the initial dip and response at 180° is equal to that of the monocular control, but all values, as in figure 6*a*,*b*, are positive.

Similar data to those of figure 6*a–d* have been collected for a population of cortical cells. Three main types of MUA responses have been found. Phase tuning which exhibits both suppression and facilitation, as in figure 6*a–d*, is one type. Second and third types show uniform suppression or facilitation, respectively, for all binocular phase values. These three types of dichoptic neural interaction have been identified in previous studies [27]. In contrast with the MUA patterns, LFP values are uniformly higher than monocular control

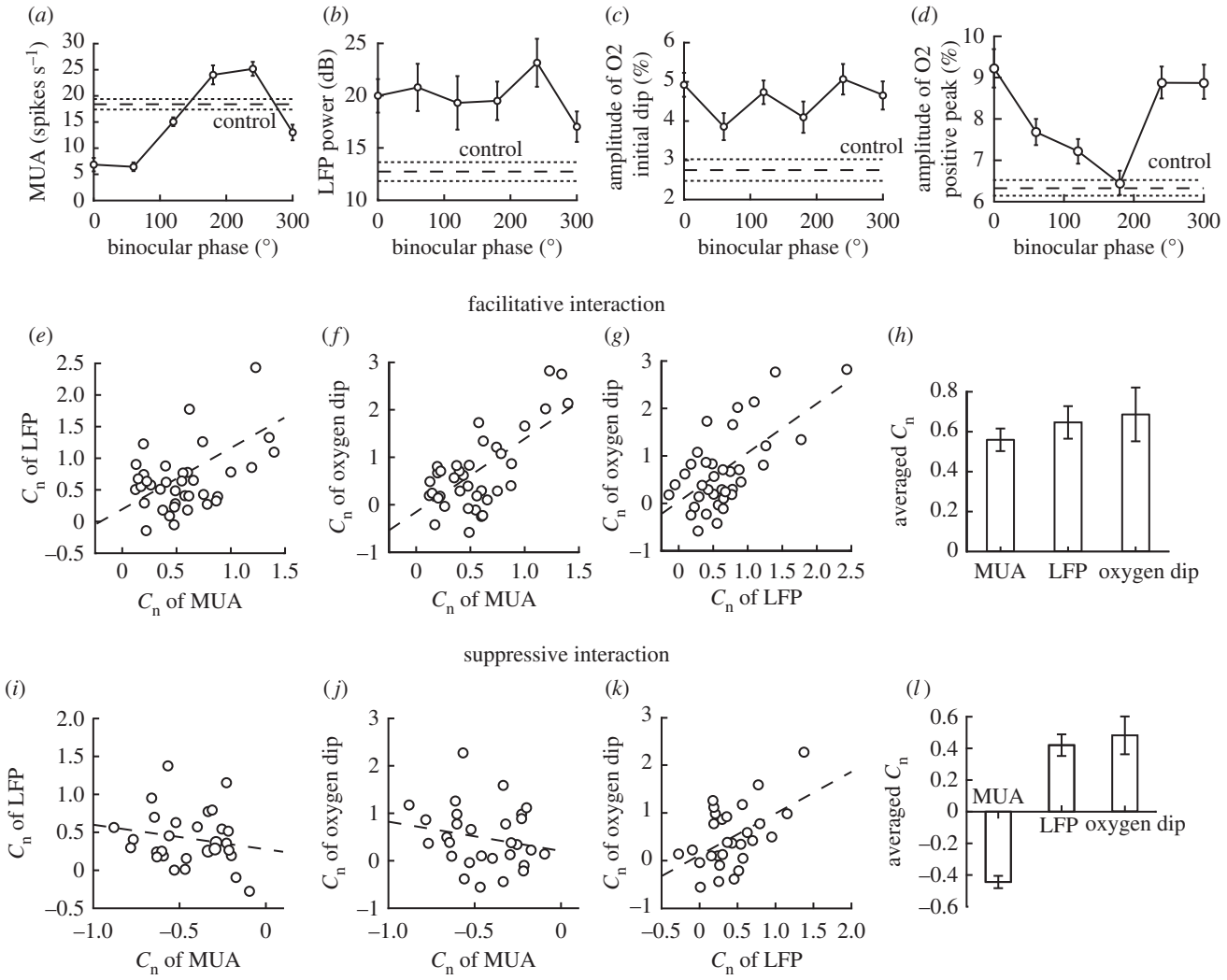

Figure 6. Binocular interaction profiles of neural and tissue oxygen responses for a representative recording site in striate cortex. (*a–d*) Averaged MUA (*a*), LFP (*b*), initial dip (*c*) and positive peak (*d*) of oxygen responses as a function of interocular spatial phase difference. Drifting sinusoidal gratings were presented to the two eyes to create interocular phase differences of: 0°, 60°, 120°, 180°, 240° and 300°. A monocular control stimulus to the dominant eye was included in the random sequence. Dashed lines in (*a–d*) represent responses to the monocular control stimulus. '0' on the horizontal axes represents onset of the visual stimulus. Data are averaged across 48 trials. Mean LFP is averaged across a frequency range of 25–115 Hz. Error bars are ±1 s.e.m. (*e–g*) Normalized changes (C_n) for MUA, LFP and initial oxygen dip for recording sites with significant excitatory (facilitative) binocular interaction ($n = 37$). Each open circle represents a recording site. Comparisons of C_n between MUA and LFP (*e*), MUA and initial oxygen dip (*f*), and LFP and initial oxygen dip (*g*), respectively. (*h*) Average C_n for MUA, LFP and initial oxygen dip. Error bars represent ±1 s.e.m. (*i–l*) Normalized changes are given for MUA, LFP and initial oxygen dip for the condition of inhibitory (suppressive) binocular interaction ($n = 29$).

results. Initial dip oxygen responses are similar to those for LFP and positive peak oxygen data appear uncoupled to both MUA and LFP. For the cell shown in figure 6*a–d*, and for other examples, MUA and LFP data are generally comparable. These variables are also consistent with initial dip oxygen results, but only during facilitative binocular interaction. During suppressive dichoptic interaction, LFP and MUA data are dissociated. In this case, LFP data and initial oxygen dips are generally associated.

Coupling characteristics between MUA, LFP, initial dip and positive peak oxygen data can be quantified as follows. Of interest is the change in relative values of monocular and binocular responses. We therefore use a normalized change index

$$C_n = \frac{R\,(\text{binoc}) - R\,(\text{monoc})}{R\,(\text{monoc})},$$

where C_n is a normalized change index; R (binoc) and R (monoc) are binocular and monocular responses, respectively; positive or negative C_n indicates excitatory or suppressive binocular interaction, respectively.

As shown above in the example of figure 6*a–d*, LFP and initial dip oxygen data change with MUA response during facilitative MUA binocular interaction, but not for that of suppression. To analyse our dataset, we compute C_n values for MUA, LFP and initial dip oxygen responses during facilitation and suppression. Results of this analysis are presented in figure 6*e–l*. For facilitative interaction, the relationships of change indices between MUA–LFP, MUA–oxygen initial dip and LFP–oxygen initial dip (figure 6*e–g*) are quite similar as the least-squares regression fits demonstrate. The histogram summary (figure 6*h*) shows similar average C_n values with no significant differences. The same data analysis for suppressive interaction has a different outcome. The relationships between MUA and LFP and MUA and oxygen dip (figure 6*i,j*) show modest negative correlations which are not significant. However, LFP is positively and significantly correlated with initial oxygen dip data (figure 6*k*). The associated averaged C_n histogram data show similar positive LFP and oxygen dip values along with a negative averaged MUA (figure 6*l*). The suppressive data shown here represent conditions in which

activation of one eye is suppressed by stimulation of the other. In this case, the suppressed MUA profile is not matched by LFP or initial oxygen dip responses. At this point, it should be noted again that the initial dip is generally not considered in fMRI work because it is weak, variable or non-existent [31,32]. However, for the preparation described here, initial dip data are reliable, consistent and generally robust. It is also well localized to the site of neural activity [30]. The analysis presented above was also made using the positive oxygen peak response instead of that of the initial dip. Positive peak data do not match alterations in LFP or MUA. However, there are similar average changes to LFP and MUA tuning during excitatory binocular response. During suppression, positive peak data are only matched to those of LFP. In summary, it is possible to examine neural–metabolic coupling during excitatory or inhibitory phases of neural activity. We have measured spiking and LFP activity during visual stimulation and associated changes in tissue oxygen at both the initial dip and positive peak levels. During excitatory binocular interaction, we find that spiking and LFP activity correlate with oxygen metabolism. Suppressive binocular interaction yields a different result. LFP and spiking activity are dissociated, but LFP and oxygen metabolism are tightly coupled. These results suggest that a similar binocular interaction paradigm should be explored in an fMRI procedure.

6. Neural activity, glucose and lactate

Neurovascular coupling involves numerous functional processes. With neural activation, there is neurotransmitter release such as glutamate and γ-aminobutyric acid. There is an increase in oxygen, glucose and ATP consumption. These events stimulate vasoactive chemical agents and metabolites that are involved in CBF. To address a part of the coupling of neural activity with energy metabolism, we have investigated the relationship between neural responses and the principal supportive substrates of glucose and lactate. We use sensors with high spatial and temporal resolution to measure simultaneous co-localized changes in glucose, lactate and neural activity in the striate cortex during visual stimulation. Electrochemical microelectrodes are used to measure tissue glucose and lactate concentration levels while neural spiking or LFP are recorded. Visual stimuli consist of gratings with optimal or contrast varying parameters [21].

The traditional view of glucose and lactate is that they are, respectively, the main neural energy substrate and the principal waste product in an associated metabolism [43]. There have been alternative views that lactate can also serve as an energy source for neurons via a glial released substrate [44,45]. This notion has been developed as the astrocyte-neuron lactate shuttle (ANLS) theory in which glucose is taken up by glial cells to produce lactate which serves to fuel neurons [44,45]. Various measurements relevant to this idea have been made [46–52] but they generally have coarse temporal or spatial resolution not suitable for capturing the rapid changes in metabolite concentration that occur during neural activity. However, electrochemical techniques have also been used which can resolve the rapid changes [53]. For the results described here, we use customized electrochemical glucose and lactate sensors combined with a neural microelectrode to determine coordinated changes in the metabolic substrates during visual activation of cortical neurons. This approach, which involves monitoring of an active *in vivo* region of cerebral cortex, is intended to reveal insights from an intact physiological system.

Representative data are presented in figure 7 for simultaneous measurements of neural activity, glucose and lactate concentration changes. Four levels of grating contrasts (10%, 20%, 40% and 80%) are used in order to explore relationships at different levels of neural activity. In figure 7*a*, a 10% contrast activation period of 30 s is shown along with a 10 s prior section which illustrates low-level spontaneous spiking. Glucose and lactate levels (figure 7*b*,*c*) are given as percentages of changes relative to the spontaneous baseline. These changes in signals are derived by averaging responses across trials. Responses are normalized and presented as percentages of signal alterations. Note that the percentage response of lactate is much larger than that of glucose. This may be accounted for by a few mechanisms. First, the baseline concentration of glucose is higher than lactate (1.1 mM and 0.05 mM, respectively) for this recording site. Second, the process of aerobic glycolysis converts one molecule of glucose to two molecules of lactate. Third, lactate might also be generated by astrocytic glycogenolysis [54,55]. What is striking in figure 7*a–c* is the consistent synchronously timed increases in MUA and lactate while glucose is simultaneously decreased. Glucose and lactate return to baseline levels immediately as neuronal activity stops. These rapid changes are not consistent with some previous reports of sustained increased lactate and decreased glucose during stimulation [53,56]. We believe the differences are due to low temporal resolution in previous work. To explore this, we reduce the temporal resolution of the analysis shown above by averaging responses of every five data points and re-plot the data of figure 7*a–c* into those given in figure 7*d–f*. These latter data now appear to show sustained changes during visual stimulation consistent with previous reports. To complete the results for all four stimulus contrast levels, mean values are presented in figure 7*g* which again shows tight coupling of neural, glucose and lactate responses. This coupling is clearly directly connected to increased neural activity as shown in figure 7*h*. We have extended these findings by use of short-duration stimuli (2 s), varied orientations including preferred and orthogonal and different visual stimulus size. Results for all the variables studied are consistent with those presented in figure 7. In summary, it is clear in an *in vivo* visual system, that there is a close temporal coordination of neural, glucose and lactate activity.

A final point of this study concerns the observation that glucose consumption is proportional to changes in CBF [1,2]. As our current results show that response profiles of glucose and lactate are tightly coordinated, we have extended this finding with simultaneous recordings of neural activity and CBF [21]. A fine laser Doppler flow needle probe with attached tungsten microelectrode is advanced into visual cortex to obtain recordings. Representative data, shown in figure 8*a*,*b*, include MUA and LFP results, respectively, which in this case are modulated in synchrony with the temporal frequency of stimulation. A very different pattern is shown for the CBF response (figure 8*c*) which consists of a sustained change during the neural response. There is also a significant temporal difference in peak changes of spiking and LFP compared with CBF signals (0.96, 0.9 and 5.34 s, respectively). In summary, the CBF signal is not synchronized with the modulation of neural activity, and there is a clear delay in the CBF signal compared with that of the neural

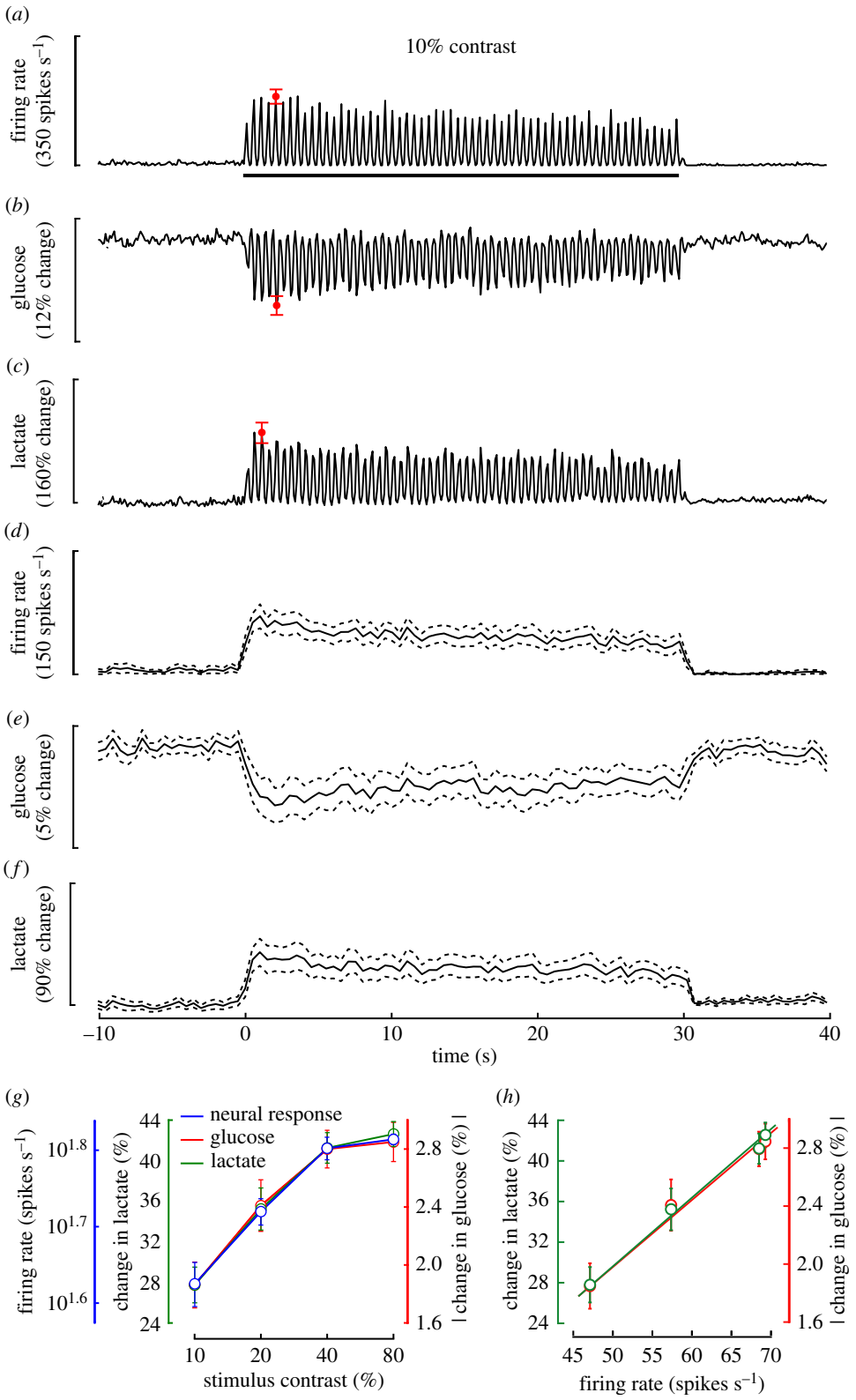

Figure 7. Neural, glucose and lactate responses to visual stimuli. (*a–c*) Neural (spike discharge) (*a*), glucose (*b*) and lactate (*c*) responses to an optimal drifting sinusoidal grating at 10% contrast for a representative recording site. Data are averaged across 16 trials. The duration of visual stimuli is 30 s. The sampling rate for spiking activity is 25 kHz while that for glucose and lactate is 10 Hz. To compare temporal coupling between neural, glucose and lactate responses to visual stimulation, spiking activity is grouped at 10 Hz. The horizontal bar in (*a*) represents stimulus onset and duration. Error bars in (*a–c*) represent the maximum ± 1 s.e.m. during visual stimulation. (*d–f*) Data in (*a–c*) are averaged across every five data points and re-plotted here. The temporal resolution is 2 Hz. (*g*) Contrast tuning functions for neural, glucose and lactate responses are given for the four contrast levels. A tight coupling is shown here between the three measurements. (*h*) Percentage changes of glucose and lactate signals are presented as a function of spiking rate. Absolute values are shown for changes in glucose responses (*g,h*). Dotted lines and error bars represent ± 1 s.e.m.

response. Consistent with our finding here, CBF signals were also reported to lag behind $CMRO_2$ and neural activity although these three measurements are linearly coupled in amplitude [40,57].

Taken together, the dynamic changes of our co-localized measurements of CBF, tissue oxygen, glucose and lactate signals are consistent with the hypothesis that lactate may serve as a mediator of metabolic information rather than as

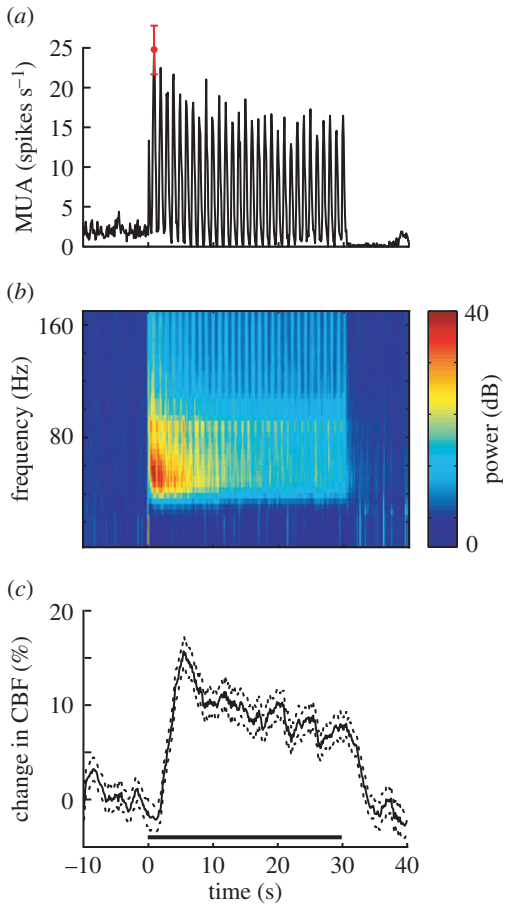

Figure 8. Simultaneous measurements of cerebral blood flow (CBF) and neural activity during presentation of optimal drifting sinusoidal grating. The stimulus size is 2°. The temporal and spatial frequencies are 1 Hz and 0.52 cycles per degree, respectively. (*a*,*b*) Neural responses exhibit a simple-cell pattern for MUA (*a*) and LFP (*b*), which show modulation in synchrony with the temporal frequency of visual stimulation. Error bar in (*a*) represents the maximum ±1 s.e.m. for MUA during visual stimulation. (*c*) CBF response to same visual stimulus. The CBF signal shows a sustained high-level change during visual stimulation. The sampling rate of the CBF signal is 10 Hz. The horizontal bar represents stimulus onset and duration (30 s). Dotted lines represent ±1 s.e.m.

a metabolic substrate, *per se* [58–60]. As neurons are activated by visual stimulation, tissue oxygen and glucose levels decrease while lactate levels increase. This is followed by blood flow rises after changes in oxygen, glucose and lactate signals. Lactate is vasoactive and dynamically alters microvasculature diameters [61]. It is likely that the lactate generated with glucose consumption may serve to maintain brain energy turnover and possibly regulate CBF. The role of lactate as an informant of metabolic states rather than as an energy substrate may help resolve the controversy over the understanding of astrocytic metabolism and its contribution to neuronal function [44,45,47,62–66]. Therefore, our results appear to be in line with a feedback mechanism in which energy supply is controlled by energy demand [30,67], rather than by a feed-forward model involving neuronal signalling via neurotransmitters [28,29,68,69].

7. Summary

The enormous potential of non-invasive neural imaging for basic and applied research and for clinical application requires clarification of acquired data. Specifically, neuronal processes must be deduced from haemodynamic measurements. Although a considerable effort has been made to clarify this transformation, fundamental questions remain. The work we describe here is an attempt to provide direct parallels between neural and haemodynamic signals. To do this, we use assessments of tissue oxygen concentration changes in cerebral cortex or the LGN while stimuli are used to activate the central visual pathway. The addition of a neural sensor provides co-localized measurements of neuronal activity. Tissue oxygen is directly related to the BOLD signal, which is the primary measurement in fMRI. It can be readily assessed by a micro-sensor in an *in vivo* preparation. This arrangement provides neural–metabolic comparisons within a functioning visual system in an anaesthetized preparation. We have utilized a variety of visual stimuli with known neural response characteristics and have also characterized co-localized changes in oxygen concentration. The typical oxygen response is bimodal with an initial negative dip followed by a large positive peak. Experimental results demonstrate that the initial dip is more reliable and a better local indicator of neural and metabolic activity than the positive peak. This finding is at odds with assessments of the initial dip in fMRI, which is considered to be unreliable. Beyond characterization, we have considered functional questions. One approach is to use a visual stimulation procedure that provides separate analysis of neural–metabolic events during suppression or facilitation. In this case, we find that LFP and spike activity are coordinated during facilitation but not in a suppression mode. In addition to the dual sensor approach, we have used an analogous system to investigate changes in primary metabolic substances, glucose and lactate, during neural activation. Results show simultaneous changes in these substances that are tightly coupled to neural activity. However, co-localized measures of CBF and neural activity show clear delays in blood flow relative to neuronal response. Although these results are significant, the relatively high temporal resolution of glucose and lactate sensors is not comparable with millisecond action potential data. We also cannot determine if generated lactate is released and consumed or transformed subsequently. And it is possible that astrocytes consume glucose for further function. These and related areas remain to be determined.

Authors' contributions. Both authors conceived the projects, performed data analysis, made the illustrations and wrote the manuscript.

Competing interests. We have no competing interests.

Funding. This work was supported by National Eye Institute Research grant no. EY01175 and CORE grant no. EY03176.

References

1. Fox PT, Raichle ME. 1986 Focal physiological uncoupling of cerebral blood flow and oxidative metabolism during somatosensory stimulation in human subjects. *Proc. Natl Acad. Sci. USA* **83**, 1140–1144. (doi:10.1073/pnas.83.4.1140)

2. Fox PT, Raichle ME, Mintun MA, Dence C. 1988 Nonoxidative glucose consumption during focal physiologic neural activity. *Science* **241**, 462–464. (doi:10.1126/science.3260686)
3. Kim SG, Ogawa S. 2012 Biophysical and physiological origins of blood oxygenation level-dependent fMRI signals. *J. Cereb. Blood Flow Metab.* **32**, 1188–1206. (doi:10.1038/jcbfm.2012.23)
4. Logothetis NK, Wandell BA. 2004 Interpreting the BOLD signal. *Annu. Rev. Physiol.* **66**, 735–769. (doi:10.1146/annurev.physiol.66.082602.092845)
5. Davis TL, Kwong KK, Weisskoff RM, Rosen BR. 1998 Calibrated functional MRI: mapping the dynamics of oxidative metabolism. *Proc. Natl Acad. Sci. USA* **95**, 1834–1839. (doi:10.1073/pnas.95.4.1834)
6. Hoge RD, Atkinson J, Gill B, Crelier GR, Marrett S, Pike GB. 1999 Linear coupling between cerebral blood flow and oxygen consumption in activated human cortex. *Proc. Natl Acad. Sci. USA* **96**, 9403–9408. (doi:10.1073/pnas.96.16.9403)
7. Kim SG, Rostrup E, Larsson HB, Ogawa S, Paulson OB. 1999 Determination of relative $CMRO_2$ from CBF and BOLD changes: significant increase of oxygen consumption rate during visual stimulation. *Magn. Reson. Med.* **41**, 1152–1161. (doi:10.1002/(SICI)1522-2594(199906)41:6<1152::AID-MRM11>3.0.CO;2-T)
8. Roland PE, Eriksson L, Stone-Elander S, Widen L. 1987 Does mental activity change the oxidative metabolism of the brain? *J. Neurosci.* **7**, 2373–2389.
9. Wey HY, Wang DJ, Duong TQ. 2011 Baseline CBF, and BOLD, CBF, and $CMRO_2$ fMRI of visual and vibrotactile stimulations in baboons. *J. Cereb. Blood Flow Metab.* **31**, 715–724. (doi:10.1038/jcbfm.2010.154)
10. Cauli B, Tong XK, Rancillac A, Serluca N, Lambolez B, Rossier J, Hamel E. 2004 Cortical GABA interneurons in neurovascular coupling: relays for subcortical vasoactive pathways. *J. Neurosci.* **24**, 8940–8949. (doi:10.1523/JNEUROSCI.3065-04.2004)
11. Enager P, Piilgaard H, Offenhauser N, Kocharyan A, Fernandes P, Hamel E, Lauritzen M. 2009 Pathway-specific variations in neurovascular and neurometabolic coupling in rat primary somatosensory cortex. *J. Cereb. Blood Flow Metab.* **29**, 976–986. (doi:10.1038/jcbfm.2009.23)
12. Kocharyan A, Fernandes P, Tong XK, Vaucher E, Hamel E. 2008 Specific subtypes of cortical GABA interneurons contribute to the neurovascular coupling response to basal forebrain stimulation. *J. Cereb. Blood Flow Metab.* **28**, 221–231. (doi:10.1038/sj.jcbfm.9600558)
13. Lee JH, Durand R, Gradinaru V, Zhang F, Goshen I, Kim DS, Fenno LE, Ramakrishnan C, Deisseroth K. 2010 Global and local fMRI signals driven by neurons defined optogenetically by type and wiring. *Nature* **465**, 788–792. (doi:10.1038/nature09108)
14. Clark Jr LC, Misrahy G, Fox RP. 1958 Chronically implanted polarographic electrodes. *J. Appl. Physiol.* **13**, 85–91.
15. Clark Jr LC, Wolf R, Granger D, Taylor Z. 1953 Continuous recording of blood oxygen tensions by polarography. *J. Appl. Physiol.* **6**, 189–193.
16. Fatt I. 1976 *Polarographic oxygen sensors*. Cleveland, OH: CRC Press.
17. Li B, Freeman RD. 2007 High-resolution neurometabolic coupling in the lateral geniculate nucleus. *J. Neurosci.* **27**, 10 223–10 229.
18. Li B, Freeman RD. 2011 Neurometabolic coupling differs for suppression within and beyond the classical receptive field in visual cortex. *J. Physiol.* **589**, 3175–3190. (doi:10.1113/jphysiol.2011.205039)
19. Li B, Freeman RD. 2012 Spatial summation of neurometabolic coupling in the central visual pathway. *Neuroscience* **213**, 112–121. (doi:10.1016/j.neuroscience.2012.04.007)
20. Li B, Freeman RD. 2013 Binocular activation elicits differences in neurometabolic coupling in visual cortex. *Neuroscience* **248**, 529–540. (doi:10.1016/j.neuroscience.2013.06.036)
21. Li B, Freeman RD. 2015 Neurometabolic coupling between neural activity, glucose, and lactate in activated visual cortex. *J. Neurochem.* **135**, 742–754. (doi:10.1111/jnc.13143)
22. Thompson JK, Peterson MR, Freeman RD. 2003 Single-neuron activity and tissue oxygenation in the cerebral cortex. *Science* **299**, 1070–1072. (doi:10.1126/science.1079220)
23. Thompson JK, Peterson MR, Freeman RD. 2004 High-resolution neurometabolic coupling revealed by focal activation of visual neurons. *Nat. Neurosci.* **7**, 919–920. (doi:10.1038/nn1308)
24. Thompson JK, Peterson MR, Freeman RD. 2005 Separate spatial scales determine neural activity-dependent changes in tissue oxygen within central visual pathways. *J. Neurosci.* **25**, 9046–9058. (doi:10.1523/JNEUROSCI.2127-05.2005)
25. Viswanathan A, Freeman RD. 2007 Neurometabolic coupling in cerebral cortex reflects synaptic more than spiking activity. *Nat. Neurosci.* **10**, 1308–1312. (doi:10.1038/nn1977)
26. Hubel DH, Wiesel TN. 1962 Receptive fields, binocular interaction and functional architecture in the cat's visual cortex. *J. Physiol.* **160**, 106–154. (doi:10.1113/jphysiol.1962.sp006837)
27. Ohzawa I, Freeman RD. 1986 The binocular organization of simple cells in the cat's visual cortex. *J. Neurophysiol.* **56**, 221–242.
28. Shen Q, Ren H, Duong TQ. 2008 CBF, BOLD, CBV, and $CMRO_2$ fMRI signal temporal dynamics at 500-msec resolution. *J. Magn. Reson. Imaging* **27**, 599–606. (doi:10.1002/jmri.21203)
29. Silva AC, Lee SP, Iadecola C, Kim SG. 2000 Early temporal characteristics of cerebral blood flow and deoxyhemoglobin changes during somatosensory stimulation. *J. Cereb. Blood Flow Metab.* **20**, 201–206. (doi:10.1097/00004647-200001000-00025)
30. Malonek D, Grinvald A. 1996 Interactions between electrical activity and cortical microcirculation revealed by imaging spectroscopy: implications for functional brain mapping. *Science* **272**, 551–554. (doi:10.1126/science.272.5261.551)
31. Buxton RB. 2001 The elusive initial dip. *NeuroImage* **13**, 953–958. (doi:10.1006/nimg.2001.0814)
32. Logothetis N. 2000 Can current fMRI techniques reveal the micro-architecture of cortex? *Nat. Neurosci.* **3**, 413–414. (doi:10.1038/74768)
33. Duong TQ, Kim DS, Ugurbil K, Kim SG. 2000 Spatiotemporal dynamics of the BOLD fMRI signals: toward mapping submillimeter cortical columns using the early negative response. *Magn. Reson. Med.* **44**, 231–242. (doi:10.1002/1522-2594(200008)44:2<231::AID-MRM10>3.0.CO;2-T)
34. Kim DS, Duong TQ, Kim SG. 2000 High-resolution mapping of iso-orientation columns by fMRI. *Nat. Neurosci.* **3**, 164–169. (doi:10.1038/72109)
35. Buxton RB. 2012 Dynamic models of BOLD contrast. *NeuroImage* **62**, 953–961. (doi:10.1016/j.neuroimage.2012.01.012)
36. Boynton GM, Engel SA, Glover GH, Heeger DJ. 1996 Linear systems analysis of functional magnetic resonance imaging in human V1. *J. Neurosci.* **16**, 4207–4221.
37. Liu H, Gao J. 2000 An investigation of the impulse functions for the nonlinear BOLD response in functional MRI. *Magn. Reson. Imaging* **18**, 931–938. (doi:10.1016/S0730-725X(00)00214-9)
38. Miller KL, Luh WM, Liu TT, Martinez A, Obata T, Wong EC, Frank LR, Buxton RB. 2001 Nonlinear temporal dynamics of the cerebral blood flow response. *Hum. Brain Mapp.* **13**, 1–12. (doi:10.1002/hbm.1020)
39. Logothetis NK, Pauls J, Augath M, Trinath T, Oeltermann A. 2001 Neurophysiological investigation of the basis of the fMRI signal. *Nature* **412**, 150–157. (doi:10.1038/35084005)
40. Sheth SA, Nemoto M, Guiou M, Walker M, Pouratian N, Toga AW. 2004 Linear and nonlinear relationships between neuronal activity, oxygen metabolism, and hemodynamic responses. *Neuron* **42**, 347–355. (doi:10.1016/S0896-6273(04)00221-1)
41. Freeman RD, Ohzawa I. 1990 On the neurophysiological organization of binocular vision. *Vis. Res.* **30**, 1661–1676. (doi:10.1016/0042-6989(90)90151-A)
42. Ohzawa I, DeAngelis GC, Freeman RD. 1990 Stereoscopic depth discrimination in the visual cortex: neurons ideally suited as disparity detectors. *Science* **249**, 1037–1041. (doi:10.1126/science.2396096)
43. Siesjo BK. 1978 *Brain energy metabolism*. New York, NY: John Wiley & Sons.
44. Magistretti PJ, Pellerin L. 1999 Astrocytes couple synaptic activity to glucose utilization in the brain. *News Physiol. Sci.* **14**, 177–182.
45. Pellerin L, Pellegri G, Bittar PG, Charnay Y, Bouras C, Martin JL, Stella N, Magistretti PJ. 1998 Evidence supporting the existence of an activity-dependent astrocyte-neuron lactate shuttle. *Dev. Neurosci.* **20**, 291–299. (doi:10.1159/000017324)
46. Fellows LK, Boutelle MG, Fillenz M. 1993 Physiological stimulation increases nonoxidative glucose metabolism in the brain of the freely moving rat. *J. Neurochem.* **60**, 1258–1263. (doi:10.1111/j.1471-4159.1993.tb03285.x)

47. Gjedde A, Marrett S. 2001 Glycolysis in neurons, not astrocytes, delays oxidative metabolism of human visual cortex during sustained checkerboard stimulation *in vivo*. *J. Cereb. Blood Flow Metab*. **21**, 1384–1392. (doi:10.1097/00004647-200112000-00002)
48. Lowry JP, O'Neill RD, Boutelle MG, Fillenz M. 1998 Continuous monitoring of extracellular glucose concentrations in the striatum of freely moving rats with an implanted glucose biosensor. *J. Neurochem.* **70**, 391–396. (doi:10.1046/j.1471-4159.1998.70010391.x)
49. Mangia S, Tkac I, Gruetter R, Van de Moortele PF, Maraviglia B, Ugurbil K. 2007 Sustained neuronal activation raises oxidative metabolism to a new steady-state level: evidence from ^{1}H NMR spectroscopy in the human visual cortex. *J. Cereb. Blood Flow Metab*. **27**, 1055–1063. (doi:10.1038/sj.jcbfm.9600401)
50. Smith D, Pernet A, Hallett WA, Bingham E, Marsden PK, Amiel SA. 2003 Lactate: a preferred fuel for human brain metabolism *in vivo*. *J. Cereb. Blood Flow Metab*. **23**, 658–664. (doi:10.1097/01.WCB.0000063991.19746.11)
51. Vlassenko AG, Rundle MM, Mintun MA. 2006 Human brain glucose metabolism may evolve during activation: findings from a modified FDG PET paradigm. *Neuroimage* **33**, 1036–1041. (doi:10.1016/j.neuroimage.2006.06.065)
52. Wyss MT, Jolivet R, Buck A, Magistretti PJ, Weber B. 2011 *In vivo* evidence for lactate as a neuronal energy source. *J. Neurosci.* **31**, 7477–7485. (doi:10.1523/JNEUROSCI.0415-11.2011)
53. Hu Y, Wilson GS. 1997 A temporary local energy pool coupled to neuronal activity: fluctuations of extracellular lactate levels in rat brain monitored with rapid-response enzyme-based sensor. *J. Neurochem.* **69**, 1484–1490. (doi:10.1046/j.1471-4159.1997.69041484.x)
54. Brown AM, Baltan Tekkok S, Ransom BR. 2004 Energy transfer from astrocytes to axons: the role of CNS glycogen. *Neurochem. Int.* **45**, 529–536. (doi:10.1016/j.neuint.2003.11.005)
55. Newman LA, Korol DL, Gold PE. 2011 Lactate produced by glycogenolysis in astrocytes regulates memory processing. *PLoS ONE* **6**, e28427. (doi:10.1371/journal.pone.0028427)
56. Caesar K, Hashemi P, Douhou A, Bonvento G, Boutelle MG, Walls AB, Lauritzen M. 2008 Glutamate receptor-dependent increments in lactate, glucose and oxygen metabolism evoked in rat cerebellum *in vivo*. *J. Physiol*. **586**, 1337–1349. (doi:10.1113/jphysiol.2007.144154)
57. Offenhauser N, Thomsen K, Caesar K, Lauritzen M. 2005 Activity-induced tissue oxygenation changes in rat cerebellar cortex: interplay of postsynaptic activation and blood flow. *J. Physiol*. **565**, 279–294. (doi:10.1113/jphysiol.2005.082776)
58. Bergersen LH, Gjedde A. 2012 Is lactate a volume transmitter of metabolic states of the brain? *Front. Neuroenergetics* **4**, 5. (doi:10.3389/fnene.2012.00005)
59. Lauritzen KH *et al.* 2014 Lactate receptor sites link neurotransmission, neurovascular coupling, and brain energy metabolism. *Cereb. Cortex* **24**, 2784–2795. (doi:10.1093/cercor/bht136)
60. Vafaee MS, Vang K, Bergersen LH, Gjedde A. 2012 Oxygen consumption and blood flow coupling in human motor cortex during intense finger tapping: implication for a role of lactate. *J. Cereb. Blood Flow Metab*. **32**, 1859–1868. (doi:10.1038/jcbfm.2012.89)
61. Gordon GR, Choi HB, Rungta RL, Ellis-Davies GC, MacVicar BA. 2008 Brain metabolism dictates the polarity of astrocyte control over arterioles. *Nature* **456**, 745–749. (doi:10.1038/nature07525)
62. Chih CP, He J, Sly TS, Roberts Jr EL. 2001 Comparison of glucose and lactate as substrates during NMDA-induced activation of hippocampal slices. *Brain Res*. **893**, 143–154. (doi:10.1016/S0006-8993(00)03306-0)
63. Dienel GA. 2012 Brain lactate metabolism: the discoveries and the controversies. *J. Cereb. Blood Flow Metab*. **32**, 1107–1138. (doi:10.1038/jcbfm.2011.175)
64. Dienel GA, Hertz L. 2001 Glucose and lactate metabolism during brain activation. *J. Neurosci. Res.* **66**, 824–838. (doi:10.1002/jnr.10079)
65. Magistretti PJ, Pellerin L, Rothman DL, Shulman RG. 1999 Energy on demand. *Science* **283**, 496–497. (doi:10.1126/science.283.5401.496)
66. Pellerin L, Magistretti PJ. 1994 Glutamate uptake into astrocytes stimulates aerobic glycolysis: a mechanism coupling neuronal activity to glucose utilization. *Proc. Natl Acad. Sci. USA* **91**, 10 625–10 629. (doi:10.1073/pnas.91.22.10625)
67. Attwell D, Laughlin SB. 2001 An energy budget for signaling in the grey matter of the brain. *J. Cereb. Blood Flow Metab*. **21**, 1133–1145. (doi:10.1097/00004647-200110000-00001)
68. Attwell D, Iadecola C. 2002 The neural basis of functional brain imaging signals. *Trends Neurosci*. **25**, 621–625. (doi:10.1016/S0166-2236(02)02264-6)
69. Uludag K, Dubowitz DJ, Yoder EJ, Restom K, Liu TT, Buxton RB. 2004 Coupling of cerebral blood flow and oxygen consumption during physiological activation and deactivation measured with fMRI. *Neuroimage* **23**, 148–155. (doi:10.1016/j.neuroimage.2004.05.013)